Applied Physics Letters

RESEARCH ARTICLE | APRIL 02 2025

Voltage-controlled half adder via magnonic inverse design

Ze Chen ; Gerard Joseph Lim ; Calvin Ching Ian Ang ; Tianli Jin ; Funan Tan ; Bryan Wei Hao Cheng ; Wen Siang Lew

Appl. Phys. Lett. 126, 132406 (2025)
https://doi.org/10.1063/5.0256599

Voltage-controlled half adder via magnonic inverse design

Cite as: Appl. Phys. Lett. **126**, 132406 (2025); doi: 10.1063/5.0256599
Submitted: 6 January 2025 · Accepted: 22 March 2025 ·
Published Online: 2 April 2025

Ze Chen, Gerard Joseph Lim, Calvin Ching Ian Ang, Tianli Jin, Funan Tan, Bryan Wei Hao Cheng, and Wen Siang Lew[a)]

AFFILIATIONS

School of Physical and Mathematical Sciences, Nanyang Technological University, 21 Nanyang Link, Singapore 637371, Singapore

[a)]Author to whom correspondence should be addressed: wensiang@ntu.edu.sg

ABSTRACT

In this work, we report a magnonic device capable of dynamic control over magnon propagation. By leveraging voltage-controlled magnetic anisotropy on yttrium iron garnet waveguides, we have carried out simulations of an active demultiplexer and half-adder designed using inverse design principles. A high output intensity multiplexer was similarly developed via inverse design to mitigate the magnon re-emission issue in Y-shaped combiners. Trapezoid electrodes were also introduced to minimize magnon intensity losses due to the magnetic anisotropy gradients across the cascading magnon circuit. The magnonic half-adder, constructed using active demultiplexers and a multiplexer, showcases the potential of magnonic logic circuits for binary addition operations.

Magnonics has emerged as a frontier field in the realm of spintronics, exploring the potential of magnons, quanta of spin waves, for information processing and computing. Unlike electrons, magnons can propagate spin information without any displacement of physical entities. Additionally, magnons have phase freedom for computing and have wavelengths ranging from micrometers to atomic scale. These features provide magnons unique advantages, such as low power consumption and high information capacity, for nanoscale data processing.[1–4]

Despite significant progress, the integration of magnonic devices into practical computing systems faces several challenges. One of the primary hurdles is the efficient control and manipulation of magnons. Traditional methods often rely on modifications to external magnetic fields[5,6] or the amplitude of magnons,[7,8] necessitating additional circuitries and greatly increasing the device footprint. Hence, both methods add complexity and energy consumption to the system. To overcome these challenges, magnetoelectric methods such as voltage-controlled magnetic anisotropy (VCMA),[9–11] electric polarization modulation in ferroelectric/ferromagnetic (FM) structures,[12] and the piezoelectric effect have been explored. VCMA enables ultrafast control of magnetic anisotropy by facilitating the accumulation or depletion of electrons.[11] Similarly, in ferrite–ferroelectric structures, the permittivity of the ferroelectric layer can be modulated by an electric field, allowing for the formation of rejection bands that facilitate magnon manipulation. However, in piezoelectric/FM bilayers, an applied electric field induces a mechanical strain in the piezoelectric layer. This strain is transferred to the adjacent FM layer, altering its magnetic properties through inverse magnetostriction. Furthermore, piezoelectric layers beneath YIG films can introduce significant strain and lattice mismatch,[13] which increase the damping constant and degrade magnon transport. Since low damping is essential for efficient spin wave propagation, the use of VCMA avoids these detrimental effects.

Previous studies had demonstrated various individual magnonic components, such as logic gates,[5,10,14–21] directional couplers,[8] and repeaters,[22] while the realization of complex computing operations using magnonics remains an active area of research. Inverse design[7] offers an automated and universal method for designing practical magnonic devices with diverse functionalities, which streamlines the design of complex magnonic devices and circuits. By combining VCMA, which provides energy-efficient dynamic control of magnons, the design of complex magnonic circuits becomes more flexible and feasible.

This work employs the inverse design technique for the development of a magnetic field-free magnonic demultiplexer, multiplexer, and a magnonic half-adder using VCMA. By using Mumax,[3] a micromagnetic simulation software,[23] we demonstrated the dynamic control capabilities of the active demultiplexer, which can guide magnon propagation by adjusting magnetic anisotropy. The magnonic half-adder, constructed using active demultiplexers and a multiplexer, showcases the potential of magnonic logic circuits for binary addition operations.

Our findings underscore significant advancements in magnonic computing, particularly in achieving highly energy-efficient signal processing.

A dual-frequency passive demultiplexer is a device that separates a mixed signal containing two distinct frequencies into two separate output channels. The top-down view of the dual-frequency passive demultiplexer is illustrated in Fig. 1(a). The demultiplexer contains one input channel, two output channels (O_1 and O_2), and a design region for guiding magnons. Within the design region, random $100 \times 100\,\text{nm}^2$ elements are removed from the waveguide to act as scattering points for the propagating magnons. The design region uses the complex scattering and interference of the magnon to route magnons to different channels based on their wavelength. The width of input and output channels is $w = 3\,\mu m$ and the waveguide thickness is maintained at $t = 100\,nm$. An excitation antenna with a width of 200 nm is positioned $10.5\,\mu$m from the design region center. The numerical simulations are performed by setting the cell size as $100 \times 100 \times 100\,\text{nm}^3$. The ferrimagnetic insulator yttrium iron garnet (YIG) with saturation magnetization $M_{sat} = 1.4 \times 10^5$ A/m, exchange stiffness $A_{ex} = 3.5 \times 10^{-12}$ J/m and damping constant $\alpha = 0.0002$ is used as a waveguide in this work.[24–27] The ultralow damping constant of the waveguide material allows magnons to propagate over dozens of micrometers, facilitating complex magnon circuits.[3,4,28] The sampling time is 100 ps limiting the derivations of magnon intensity from 0 to 5 GHz with fast Fourier transform (FFT). For the simultaneous excitation of dual magnon frequencies f_1 and f_2, the excitation magnetic field $B_x = 0.1\sin(2\pi f_1 t) + 0.1\sin(2\pi f_2 t)\,mT$ was applied. An out-of-plane external field with an amplitude of $B_z = 0.2\,T$ was applied along the positive z direction, resulting in forward volume magnetostatic waves (FVMSW). High damping regions with a damping constant of 1, are placed at the terminations of the input and output channels to mitigate magnon reflections.[29]

The inverse design procedure, as depicted in Fig. 1(b), iteratively modifies the device structure using Monte Carlo simulations. In each iteration, ten elements within the design region are randomly altered. The objective function, O, is defined as follows:

$$O = (I_{f_1,O_1} - I_{f_1,O_2}) * (I_{f_2,O_2} - I_{f_2,O_1}),$$

where I_{f_i,O_i} indicates the intensity of frequency f_i at output O_i. This objective function evaluates the degree of distinction between the output intensities of the two predefined frequencies. In this work, two frequencies of 1 and 1.2 GHz were studied. If the objective function value increases compared to the previous iteration, the modified design region is retained. Otherwise, further changes are made based on the previous structure with the highest objective function. This iterative process repeats until the objective function converges, signifying the identification of an optimized device structure. The inverse design approach for a passive demultiplexer seeks for a structure that causes destructive interference of specific frequencies at one output port with a simultaneous constructive interference at the other port, thereby achieving frequency-based signal routing.

As shown in Fig. 1(c), convergence was clearly observed after 3000 iterations, achieving the highest objective function value (9.2) at iteration 2603. The non-overlapping transmission peaks in Fig. 1(d) demonstrate their effectiveness as a magnonic passive demultiplexer. The demultiplexer design can also be optimized to accommodate only frequencies beyond the demonstrated predefined values of 1.0 and 1.2 GHz. Demultiplexers for various frequencies of multifrequency

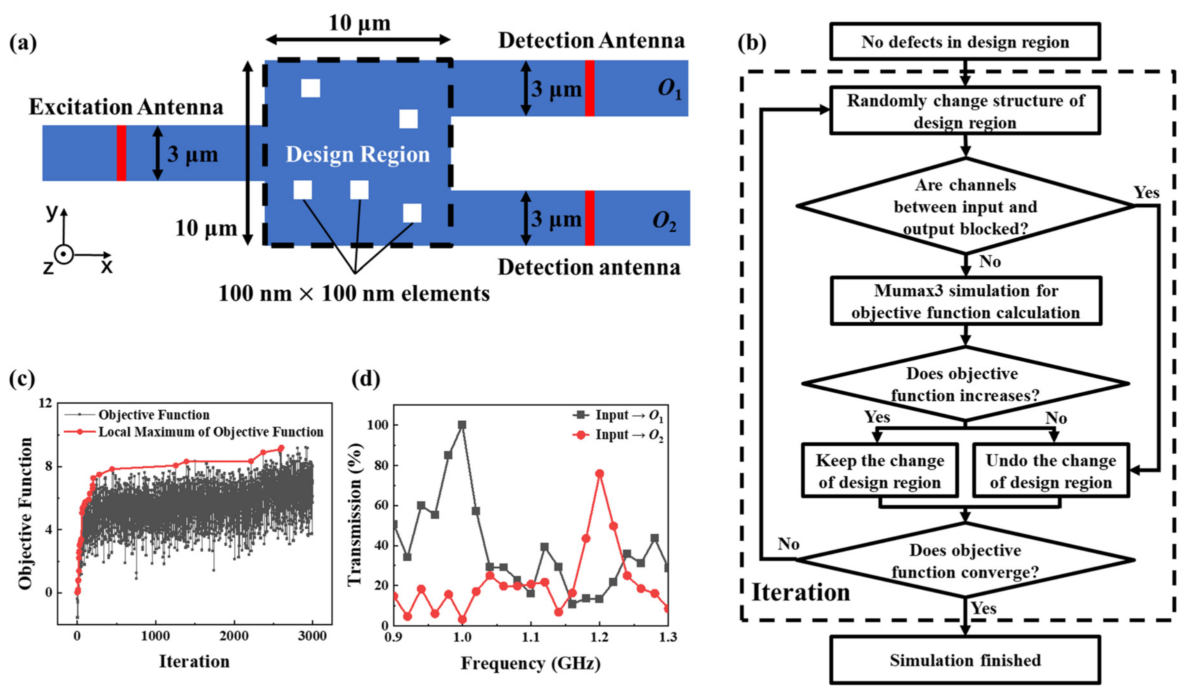

FIG. 1. (a) Schematic of the demultiplexer structure. (b) Flowchart of inverse design process. (c) Objective function value vs iteration, achieving its highest value at iteration 2603. (d) Transmission spectrum of a magnonic passive demultiplexer.

applications can be obtained simply by repeating the process laid out in Fig. 1(b) with their corresponding objective functions.

The field-free active demultiplexer with VCMA enables dynamic control over the waveguide magnetic anisotropy, enabling manipulation of magnon dispersion relation and the wavelength dependent demultiplexing. The dispersion relation is obtained by generating broadband magnons using a *sinc* function $B_X = b_0 \mathrm{sinc}(2\pi f_c(t - t_0))$, where b_0, f_c, and t_0 are the pulse amplitude, cutoff frequency, and central time of the pulse, respectively. A two-dimensional fast Fourier transform (2D FFT) is performed to obtain 3D dispersion relation map along the middle line of the waveguide and on the time evolution. The lowest collective magnon mode was obtained with the frequency that has the highest amplitude for each wavevector.[30,31] For the active magnonic demultiplexer, the design region within the device remains identical to the passive demultiplexer. The out-of-plane external field previously used to align the magnetization along the z axis was removed and a first-order uniaxial anisotropy constant K_u along the z axis was introduced to realize a field-free device. Experimental realization of such a device can be achieved by YIG doping.[32,33] The VCMA effect was emulated by dynamically adjusting the value of K_u in Mumax.[3] VCMA utilizes an electric field generated by a top Au electrode and a bottom Cu electrode to adjust the K_u of the device,[34] as depicted in Fig. 2(a).

The previous passive demultiplexer had been optimized for the demultiplexing of the wavelengths corresponding to 1 and 1.2 GHz magnons under a 0.2 T out-of-plane magnetic field. The removal of the out-of-plane magnetic field and the introduction of an out-of-plane magnetic anisotropy in the active demultiplexer causes a change in the magnon dispersion relation and wavelength. Thus, new conditions to tune the magnon wavelength to match that of the previous passive demultiplexer are required. By investigating the device objective function for a range of K_u without any external field, the K_u of 13 990 J/m^3 was found to be optimal for 1 and 1.2 GHz demultiplexing (see supplementary material Fig. S1). In other words, the K_u of 13 990 J/m^3 provides the dispersion relation that most closely matches the magnon wavelengths of the 1 and 1.2 GHz magnons that were found in the passive demultiplexer.

Advancing from demultiplexing between 1 and 1.2 GHz between the two outputs in the passive demultiplexer, the active demultiplexer functions to demultiplex a single frequency magnon between the two outputs by tuning their dispersion relation via manipulating magnetic anisotropy. Figure 2(b) demonstrates the effective demultiplexing of 1.0 GHz magnons, as seen from the positive peak and negative troughs at distinct K_u values. The negative K_u trough at 13 500 J/m^3 corresponds to the optimal anisotropy to divert the 1 GHz magnons to O_2, as shown in Fig. 2(c). The positive K_u peak at 13 990 J/m^3 corresponds to the optimal anisotropy to divert the 1 GHz magnons to O_1, as shown in Fig. 2(d). Additionally, at K_u of 13 990 J/m^3 the O_1 - O_2 peak of the 1 GHz magnon aligns with the trough of the 1.2 GHz magnon, demonstrating the retained passive demultiplexing of the 1 and 1.2 GHz magnons for this specific K_u.

As mentioned in the above discussion, both the magnon frequency and the magnetic anisotropy affect the wavelengths of the magnons and thus the demultiplexing effects on the device. In this inverse designed device, the optimal wavevector for the demultiplexing of magnons to O_1 and O_2 are 0.50 and 0.89 μm^{-1}, respectively. The color map in Fig. 2(e) shows how both K_u and frequency modulate the wavevector, which underlies the change in propagation direction. Figure 2(f) shows that tuning K_u via the VCMA effect allows precise control of the resonant magnon frequency at outputs O_1 and O_2. This enables effective spin wave routing based on frequency. It indicates that for a particular K_u value, the device would be optimal to split the

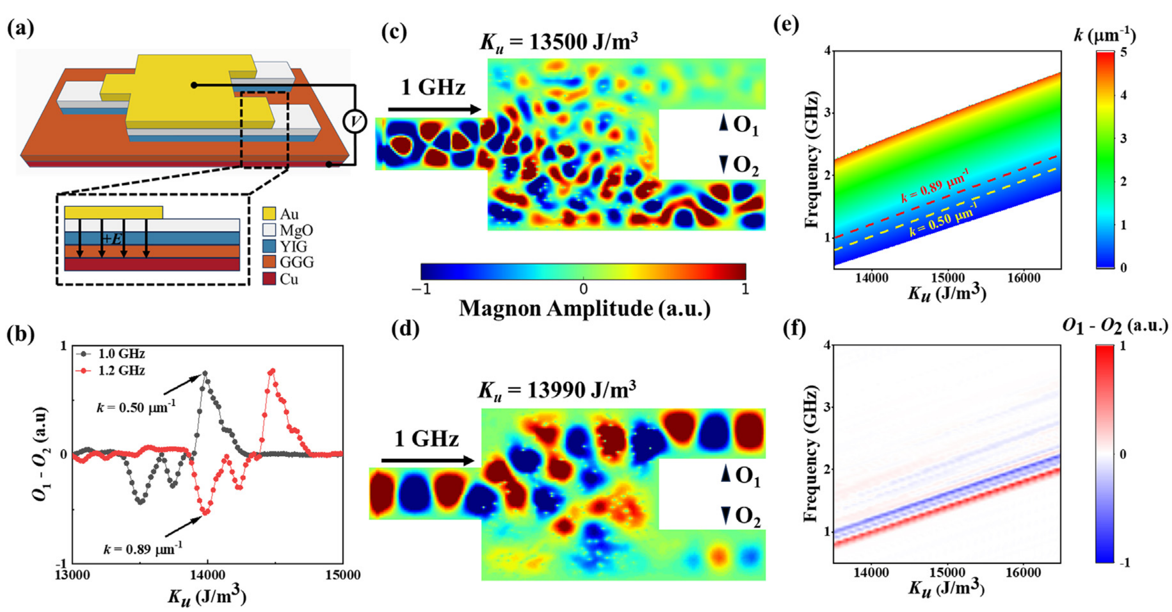

FIG. 2. (a) Schematic of the active demultiplexer structure with VCMA. Thickness of the individual layers are not drawn to scale. (b) Output intensity of $O_1 - O_2$ with different K_u values for 1 and 1.2 GHz magnons. (c) Simulated magnon amplitude distribution of 1 GHz input with $K_u = 13\,500$ J/m^3. (d) Simulated magnon amplitude distribution of 1 GHz input with $K_u = 13\,990$ J/m^3. (e) Wavevector of magnons influenced by frequency and K_u. (f) $O_1 - O_2$ influenced by frequency and K_u.

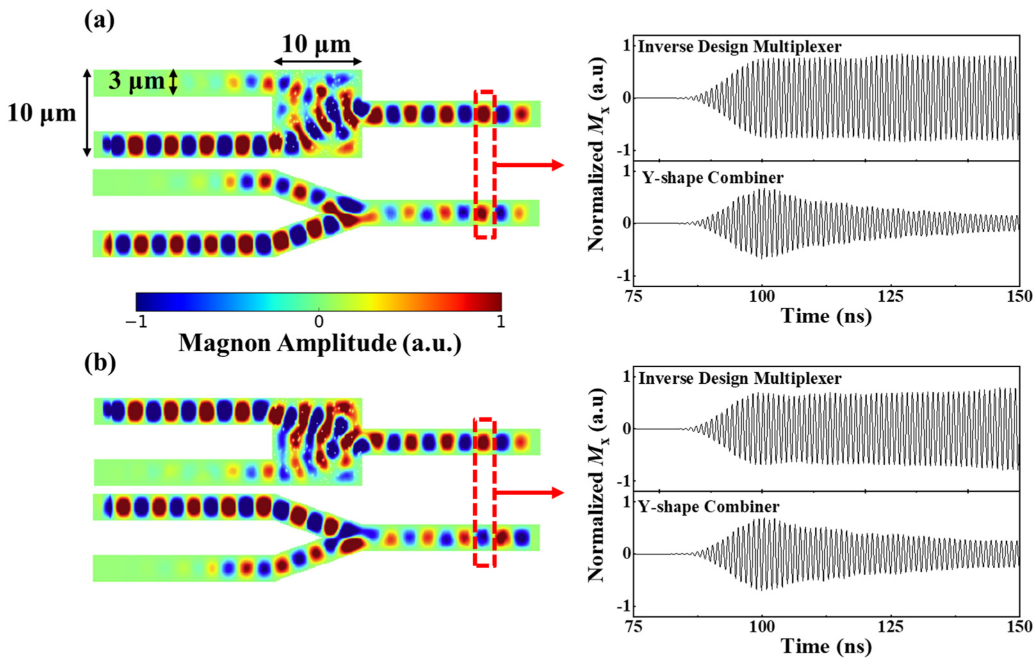

FIG. 3. (a) Simulated magnon amplitude map and output signal when the magnon source is at lower input channel. (b) Magnon amplitude map and output signal when the magnon source is at the upper input channel.

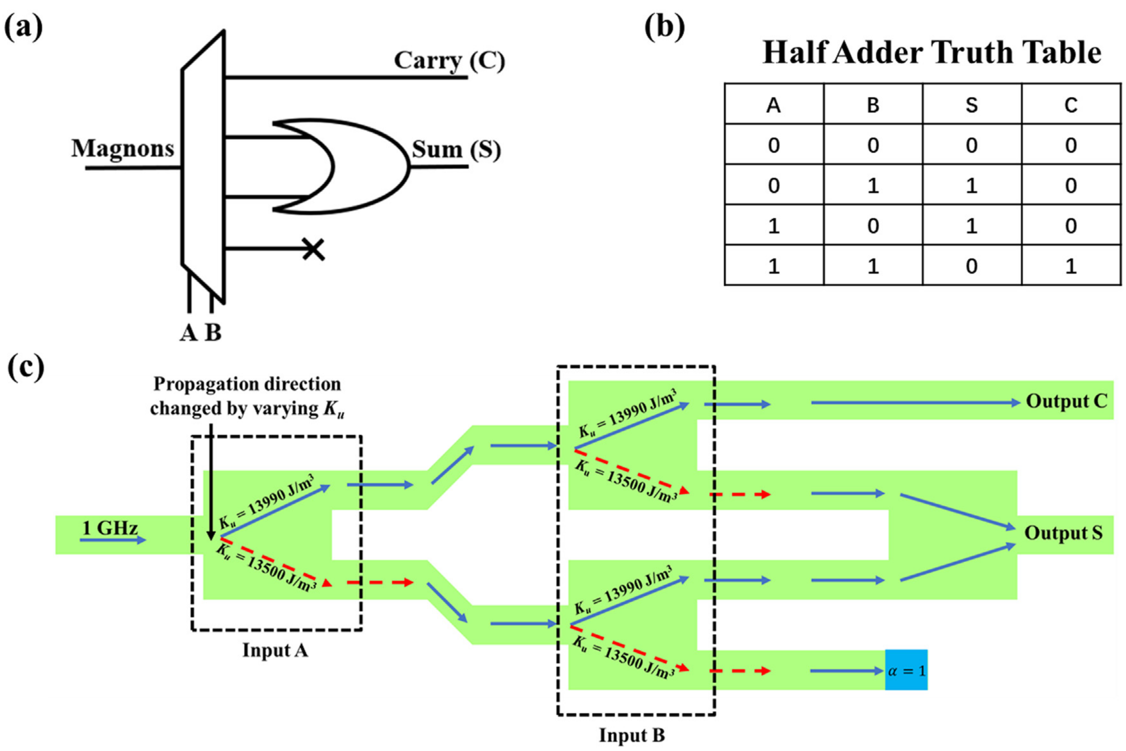

A	B	S	C
0	0	0	0
0	1	1	0
1	0	1	0
1	1	0	1

FIG. 4. (a) Structure of magnonic half adder in electronics format. (b) Truth table of a half adder. (c) Structure of magnonic half adder built by 3 demultiplexers and 1 multiplexer.

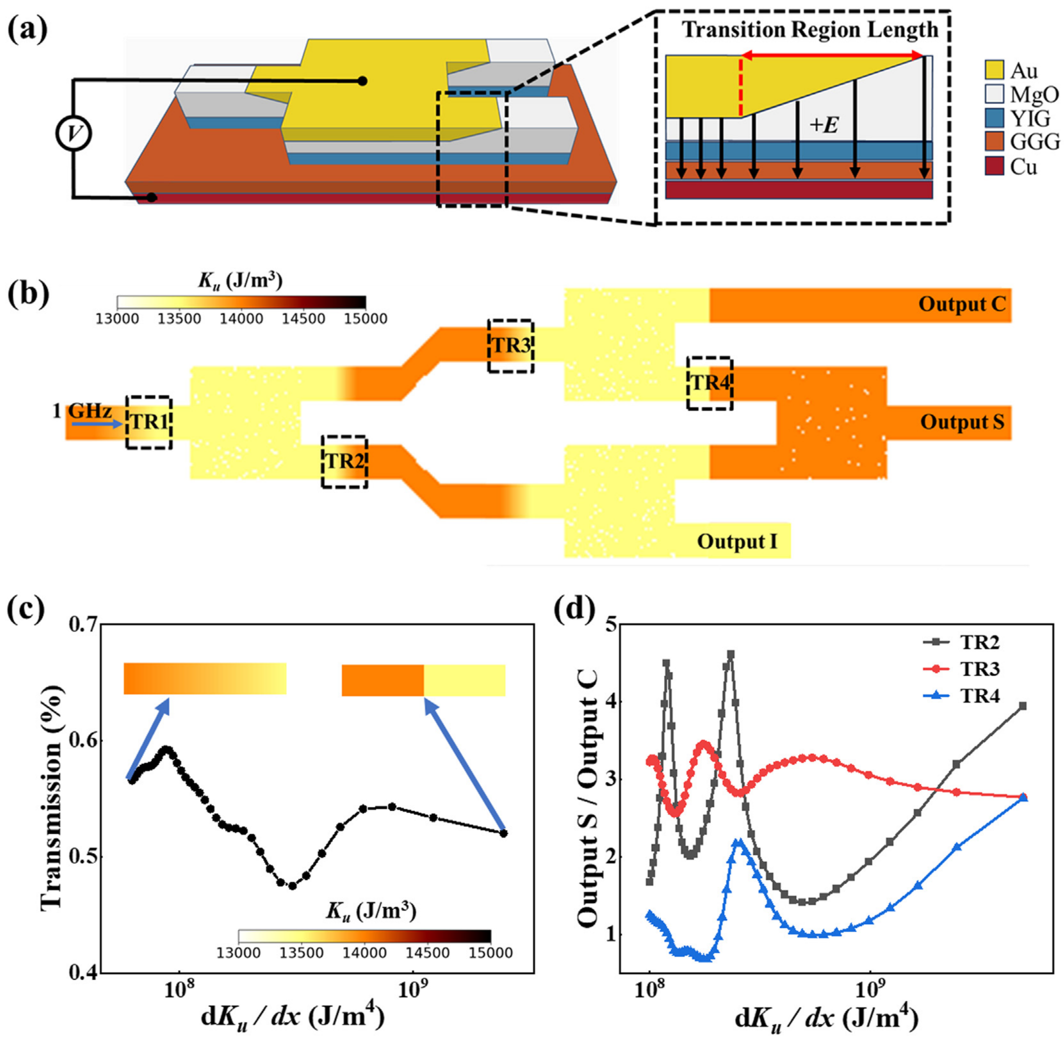

FIG. 5. (a) Schematic of the active demultiplexer structure with VCMA and trapezoid-shape electrodes. (b) Simulated K_u distribution of magnonic half adder when inputs are "0" and "0" (13 500 J/m^3 for inputs A and B). (c) Transmission rate for magnon propagating from 13 990 to 13 500 J/m^3 with respect to the dK_u/dx in stripe line waveguide. (d) Output S/output C (logic "1"/logic "0" ratio) vs dK_u/dx for transition regions 2, 3, and 4, respectively.

two frequencies corresponding to the maximum and minimum O_1 - O_2. Additionally, for a particular frequency, the device can also direct the magnons to distinct directions between two K_u values.

The function of an OR gate is to output a logic "1" signal if there is at least one input logic "1" signal, which can be simply realized by merging two channels like a Y-shaped combiner. However, a major issue of magnon combiners is the coexistence of multiple magnon modes with varying wavelengths at the same frequency. Irregularities in the combiner region, often act as sources that generate additional magnons of the same frequency but with different wavenumbers.[17,31,35] Inverse design provides a solution for this re-emitting problem by replacing the combiner with a multiplexer. As shown in Fig. 3(a), the multiplexer has two input channels, one output channel, and one design region. The width of the input channel and the output channel is 3 μm, and the design region is 10 $\times$ 10 μm^2. The magnetic anisotropy of the multiplexer is set as $K_u = 13\,990$ J/m^3. Two antennas are placed at two input channels, respectively, generating 1 GHz magnons simultaneously. Following the procedure established for the demultiplexer, an inverse design was applied to the multiplexer, optimizing for 1 GHz magnon intensity at the output port. The convergence can be observed after 300 iterations (see supplementary material Fig. S2). The comparison in magnon intensity for the cases of single logic "1" input are shown in Figs. 3(a) and 3(b). A clear improvement in magnon intensity of approximately 300% was achieved by the proposed multiplexer compared to a Y-shaped combiner.

The structure of a magnonic half adder is based on the electronic half adder, comprising a 2 $\times$ 4 active demultiplexer and an OR gate, as shown in Fig. 4(a). The truth table of the half adder is depicted in Fig. 4(b), while the complete structure of the magnonic half adder is illustrated in Fig. 4(c). The 2 $\times$ 4 magnonic active demultiplexer is

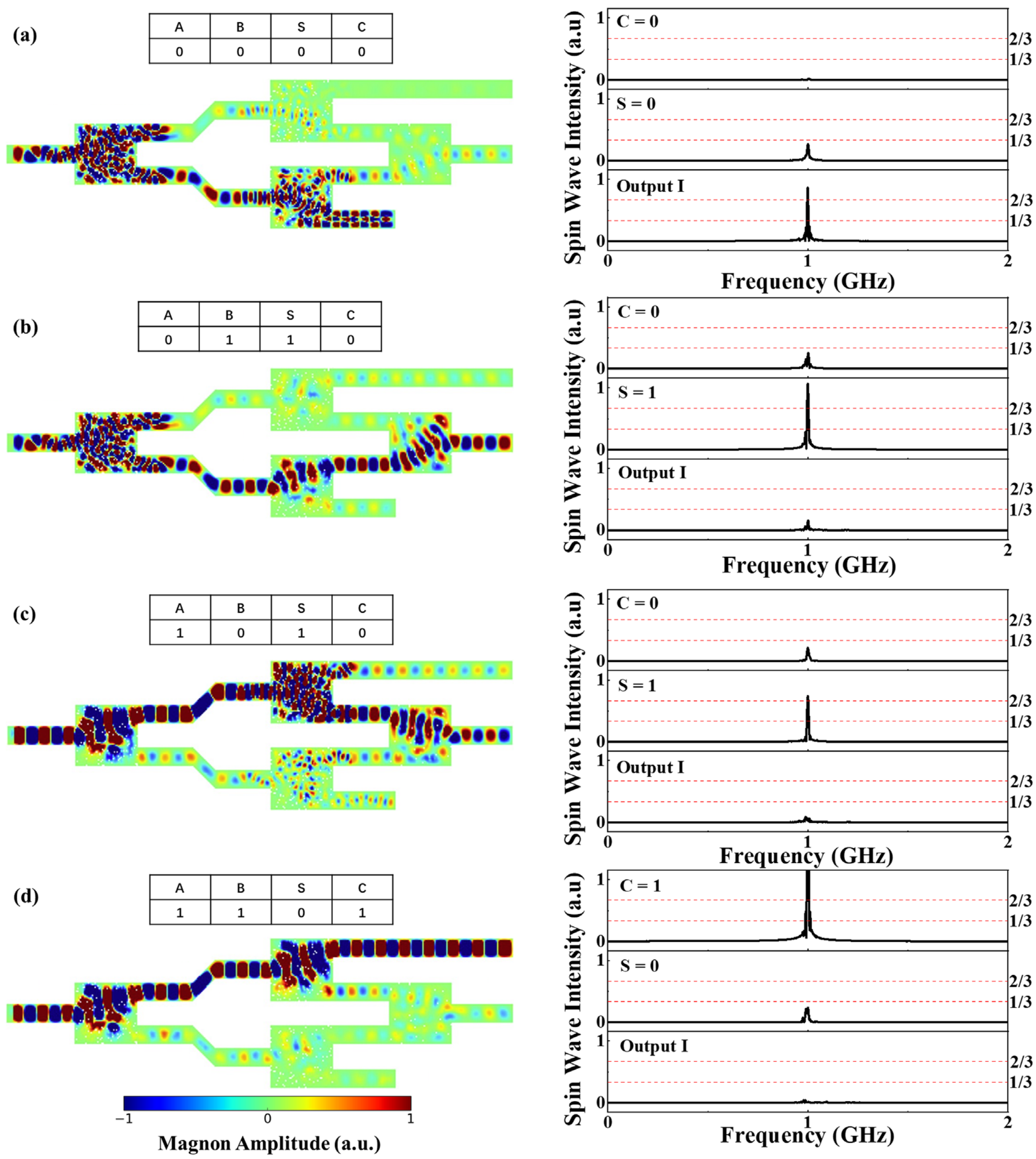

FIG. 6. Simulated magnon intensity map for different inputs: (a) A = 0, B = 0, (b) A = 0, B = 1 (c) A = 1, B = 0, and (d) A = 1, B = 1.

realized using three active demultiplexers and a multiplexer that functions as the OR gate. The whole waveguide has a magnetic anisotropy $K_u = 13\,990\ \mathrm{J/m^3}$ when no voltage or VCMA effect is applied. A logical input of "0" is applied across the demultiplexers as a decrement of K_u to $13\,500\ \mathrm{J/m^3}$ while employing a VCMA effect, which drives magnons to the lower output port. Conversely, no VCMA is applied for the logical input of "1," which results in the device with a higher $K_u = 13\,990\ \mathrm{J/m^3}$ and driving magnons to the upper output port.

However, magnon reflection is found at the boundaries with an abrupt change in magnetic anisotropy and dispersion relation mismatch.[36] The reflection will decrease the digitalization at the output port, i.e., the ratio of output signal intensity for logic "1" to logic "0." Hence, trapezoid-shape electrodes[37–39] are utilized at both input and output for each active demultiplexer, as shown in Fig. 5(a). The transition region (TR) length is defined by the red arrow in the inset of Fig. 5(a). The trapezoidal shape is formed with a varying MgO thickness between the top electrode and YIG waveguide, where a gradual change in K_u along the channel is formed to reduce magnon reflection.

The abrupt K_u boundaries only occur for the case of logic "0," where VCMA is applied. For logic inputs A = 1 and B = 1, the K_u across the entire waveguide is uniform at 13 990 J/m^3 and does not have magnon reflection issues. For logic inputs A = 0 and B = 0, the magnons are directed downward to output I, where the magnon intensity data are discarded and not used for computation; thus, no optimization of the bottom demultiplexer at input B is required. For both logic input A = 0, B = 1 and logic input A = 1, B = 0, the logic outputs are S = 1 and C = 0, the digitalization can be measured by the output S/output C ratio. The optimization is achieved by adjusting the length of the TR, which directly modifies $\frac{dK_u}{dx}$. The locations of the TRs are indicated in Fig. 5(b). TR1 and TR2 refer to logic input A = 0, B = 1, while TR3 and TR4 refer to logic input A = 1, B = 0. For TR1, magnons propagate from a K_u region of 13 990–13 500 J/m^3 in the stripe line waveguide. The relation of transmission and average $\frac{dK_u}{dx}$ is presented in Fig. 5(c). The length of TR1 is chosen to be 5.6 μm because the maximum transmission rate is achieved with this length. For TR2, the output S/output C ratio with respect to average $\frac{dK_u}{dx}$ is investigated, as shown in Fig. 5(d), which achieves maximum value when the length of the transition region is 2.1 μm. Thus, the length of TR2 is chosen as 2.1 μm. Similar investigations are performed for TR3 and TR4. The lengths of TR3 and TR4 are chosen as 2.8 and 0.1 μm, respectively.

With the application of the trapezoidal electrodes, the magnon intensity and output intensity at each output port are shown in Fig. 6. The magnon intensity map for each half-adder configuration is presented, validating the proposed design. The frequency spectra of the three output ports for all four cases are also provided. An output magnon intensity exceeding 2/3 is interpreted as a logical "1," while an intensity below 1/3 represents a logical "0."

In conclusion, we have demonstrated the functionality of both passive and active magnonic frequency demultiplexers, as well as a magnonic multiplexer. When combined, these components enable a functionary magnonic half adder, all leveraging VCMA in YIG waveguides. The magnetic field-free demultiplexer exhibits dynamic control capabilities, enabling the routing of magnons based on frequency by adjusting magnetic anisotropy. The multiplexer mitigates re-emission of magnons in the conventional Y-shaped combiner. The magnonic half-adder, demonstrates binary addition operations, showcasing the potential for energy-efficient magnonic logic circuits in advanced computing. These findings contribute to the better understanding of magnonic device technology, specifically for achieving low-power signal processing applications.

See the supplementary material for analyses of the objective function with magnetic anisotropy and iterative convergence of a 1 GHz magnonic multiplexer.

This work was supported by a RIE2020 ASTAR AME IAF-ICP Grant No. I1801E0030 and a MOE Tier 1 grant (No. RG76/23).

AUTHOR DECLARATIONS

Conflict of Interest

The authors have no conflicts to disclose.

Author Contributions

Ze Chen: Conceptualization (lead); Data curation (lead); Formal analysis (lead); Investigation (lead); Methodology (lead); Software (lead); Validation (lead); Visualization (lead); Writing – original draft (lead). **Gerard Joseph Lim:** Conceptualization (equal); Software (equal); Writing – review & editing (equal). **Calvin Ching Ian Ang:** Software (equal); Validation (equal); Writing – review & editing (equal). **Tianli Jin:** Methodology (equal); Visualization (equal); Writing – review & editing (equal). **Funan Tan:** Data curation (equal); Methodology (equal); Software (equal); Writing – review & editing (equal). **Bryan Wei Hao Cheng:** Investigation (equal); Writing – review & editing (equal). **Wen Siang Lew:** Funding acquisition (equal); Project administration (equal); Resources (equal); Supervision (equal); Writing – review & editing (equal).

DATA AVAILABILITY

The data that support the findings of this study are available from the corresponding author upon reasonable request.

REFERENCES

[1]P. Pirro, V. I. Vasyuchka, A. A. Serga, and B. Hillebrands, Nat. Rev. Mater. **6**, 1114–1135 (2021).
[2]G. Finocchio, J. A. C. Incorvia, J. S. Friedman, Q. Yang, A. Giordano *et al.*, Nano Futures **8**, 012001 (2024).
[3]Q. Wang, G. Csaba, R. Verba, A. V. Chumak, and P. Pirro, Phys. Rev. Appl. **21**, 040503 (2024).
[4]B. Flebus, D. Grundler, B. Rana, Y. C. Otani, I. Barsukov *et al.*, J. Phys. Condens. Matter **36**, 363501 (2024).
[5]K. S. Lee and S. K. Kim, J. Appl. Phys. **104**, 053909 (2008).
[6]A. Khitun, M. Bao, and K. L. Wang, J. Phys. D **43**, 264005 (2010).
[7]Q. Wang, A. V. Chumak, and P. Pirro, Nat. Commun. **12**, 2636 (2021).
[8]Q. Wang, M. Kewenig, M. Schneider, R. Verba, F. Kohl *et al.*, Nat. Electron. **3**(12), 765–774 (2020).
[9]B. Rana, Commun. Phys. **2**, 90 (2019).
[10]B. Rana and Y. Otani, Phys. Rev. Appl. **9**, 14033 (2018).
[11]B. Rana, J. Appl. Phys. **136**, 150701 (2024).
[12]H. Qin, R. Dreyer, G. Woltersdorf, T. Taniyama, and S. van Dijken, Adv. Mater. **33**, 1–9 (2021).
[13]M. J. Gross, W. A. Misba, K. Hayashi, D. Bhattacharya, D. B. Gopman, J. Atulasimha, and C. A. Ross, Appl. Phys. Lett. **121**, 252401 (2022).
[14]A. V. Chumak, A. A. Serga, and B. Hillebrands, Nat. Commun. **5**, 4700 (2014).
[15]A. Khitun and K. L. Wang, J. Appl. Phys. **110**, 034306 (2011).
[16]S. Klingler, P. Pirro, T. Brächer, B. Leven, B. Hillebrands, and A. V. Chumak, Appl. Phys. Lett. **105**, 152410 (2014).
[17]S. Klingler, P. Pirro, T. Brächer, B. Leven, B. Hillebrands, and A. V. Chumak, Appl. Phys. Lett. **106**, 212406 (2015).
[18]G. Talmelli, T. Devolder, N. Träger, J. Förster, S. Wintz *et al.*, Sci. Adv. **6**, eabb4042 (2020).
[19]K. Ganzhorn, S. Klingler, T. Wimmer, S. Geprägs, R. Gross, H. Huebl, and S. T. B. Goennenwein, Appl. Phys. Lett. **109**, 022405 (2016).
[20]K. Vogt, F. Y. Fradin, J. E. Pearson, T. Sebastian, S. D. Bader, B. Hillebrands, A. Hoffmann, and H. Schultheiss, Nat. Commun. **5**, 3727 (2014).
[21]K. Baumgaertl and D. Grundler, Appl. Phys. Lett. **118**, 162402 (2021).
[22]Q. Wang, R. Verba, K. Davídková, B. Heinz, S. Tian, Y. Rao, M. Guo, X. Guo, C. Dubs, P. Pirro, and A. V. Chumak, Nat. Commun. **15**, 7577 (2024).
[23]A. Vansteenkiste, J. Leliaert, M. Dvornik, M. Helsen, F. Garcia-Sanchez, and B. Van Waeyenberge, AIP Adv. **4**, 107133 (2014).
[24]R. Schlitz, T. Helm, M. Lammel, K. Nielsch, A. Erbe, and S. T. B. Goennenwein, Appl. Phys. Lett. **114**, 252401 (2019).
[25]S. Klingler, A. Chumak, T. Mewes, B. Khodadadi, C. Mewes, C. Dubs, O. Surzhenko, B. Hillebrands, and A. Conca, J. Phys. D: Appl. Phys. **48**, 1–5 (2015).

[26]H. Chang, P. Li, W. Zhang, T. Liu, A. Hoffmann, L. Deng, and M. Wu, IEEE Magn Lett **5**, 1–4 (2014).
[27]C. Dubs, O. Surzhenko, R. Thomas, J. Osten, T. Schneider, K. Lenz, J. Grenzer, R. Hübner, and E. Wendler, Phys. Rev. Mater. **4**, 024416 (2020).
[28]A. A. Serga, A. V. Chumak, and B. Hillebrands, J. Phys. D **43**, 264002 (2010).
[29]G. Venkat, H. Fangohr, and A. Prabhakar, J. Magn. Magn. Mater. **450**, 34–39 (2018).
[30]M. G. Copus, A. R. Stuart, R. E. Camley, and K. S. Buchanan, J. Appl. Phys. **132**, 123901 (2022).
[31]Q. Wang, P. Pirro, R. Verba, A. Slavin, B. Hillebrands, and A. V. Chumak, Sci. Adv. **4**, e1701517 (2018).
[32]L. Soumah, N. Beaulieu, L. Qassym, C. Carrétéro, E. Jacquet, R. Lebourgeois, J. Ben Youssef, P. Bortolotti, V. Cros, and A. Anane, Nat. Commun. **9**, 3355 (2018).
[33]J. Ding, C. Liu, Y. Zhang, U. Erugu, Z. Quan *et al.*, Phys. Rev. Appl. **14**, 014017 (2020).
[34]X. Zhang, T. Liu, M. E. Flatté, and H. X. Tang, Phys. Rev. Lett. **113**, 037202 (2014).
[35]M. Balynsky, D. Gutierrez, H. Chiang, A. Kozhevnikov, G. Dudko, Y. Filimonov, A. A. Balandin, and A. Khitun, Sci. Rep. **7**, 11539 (2017).
[36]Q. Wang, T. Brächer, M. Fleischhauer, B. Hillebrands, and P. Pirro, Appl. Phys. Lett. **118**, 182404 (2021).
[37]F. N. Tan, W. L. Gan, C. C. I. Ang, G. D. H. Wong, H. X. Liu, F. Poh, and W. S. Lew, Sci. Rep. **9**, 7369 (2019).
[38]X. Wang, W. L. Gan, J. C. Martinez, F. N. Tan, M. B. A. Jalil, and W. S. Lew, Nanoscale **10**, 733–740 (2018).
[39]C. C. I. Ang, W. Gan, and W. S. Lew, New J. Phys. **21**, 043006 (2019).